High repetition rate femtosecond laser heat accumulation and ablation thresholds in cobalt-binder and binderless tungsten carbides

Kendrick Mensink, Elías H. Penilla, Pablo Martínez-Torres, Natanael Cuando-Espitia, Suveen Mathaudhu*, Guillermo Aguilar*

Department of Mechanical Engineering, University of California, Riverside, CA, 92521, USA

A B S T R A C T

Femtosecond (fs) laser ablation has been studied for the potential of fast, high precision machining of difficult-to-machine materials like binderless tungsten carbide. Obstacles that have limited its efficiency include melting from heat accumulation (HA), particle shielding, and plasma shielding. To address HA without shielding effects, high repetition rate (57.4 MHz), ultra-low fluence fs laser irradiation is performed to study the incubation effect and subsequent HA-ablation threshold of fine-grained tungsten carbides. Exposure times on the order of 100 ms were conducted in air with fluences (1.82 to 9.09 mJ/cm^2) two orders of magnitude below the single fs pulse ablation thresholds reported in literature (0.4 J/cm^2). Heat accumulation at high repetition rate explains the ultra-low fluence melt threshold behavior resulting in melt crowns around ablated holes and grooves. The results of this study aid in predicting heat buildup in high repetition rate laser irradiation for applications that wish to achieve high ablation rates of difficult-to-machine, ultrahard materials and help enable shaping of binderless tungsten carbide for use in applications too extreme for bindered tungsten carbide.

1. Introduction

Lasers are increasingly useful for a variety of materials processing techniques including marking, cutting, biocompatible surfacing, and other types of surface modification and micromachining. Among the main advantages of laser material processing are localized precision processing and fast processing times for creating surface features on the micrometer (μm) scale. Sugioka and Cheng (2014) have noted how femtosecond (fs) lasers in particular have revolutionized material processing in a variety of applications, in part due to the minimized heat affected zone when ablating or vaporizing many materials. Therefore, ultrashort pulsed lasers are good candidates for controlling the topologies and properties of select surfaces while not significantly affecting nearby material properties. Echlin et al. (2015) have shown them to be effective for fast, layer-by-layer ablation with minimal or no associated damage, while Farsari et al. (2007) have demonstrated four orders of magnitude increase in laser scribing speed of silicon carbide by using unamplified high repetition rate (50 MHz) compared to amplified kHz systems.

Tungsten carbide (WC) is a high-density material that is used in armor piercing ammunition, cutting tools and applications requiring high hardness or high temperatures. To increase formability and toughness a metallic binder, frequently cobalt (Co), is used, although at the expense of tool hardness. Despite binderless WC having superior performance to its bindered counterpart in high temperature, high pressure applications, binderless WC has been less studied than bindered WC because of its limited formability. Because both binderless WC and bindered WC are very hard relative to other cutting materials, Jahan et al. (2011) have shown wire electro-discharge machining (EDM) to be an effective tool for simple or complex shaping of WC. With EDM however, complex shapes require complex dies, and electrodes are required regardless of the geometric complexity. For hard polycrystalline materials that are not amenable to photolithographic machining approaches, laser machining is one of very few techniques to remove small volumes at less than 50 μm resolution and with fast material removal rates. Thus Eberle and Wegener (2014) explored picosecond (ps) and nanosecond (ns) laser machining of WC and diamond, as an alternative method to EDM. EDM has limitations of electrode wear, machining only conductive samples and complicated sample fixturing within dielectric medium. A further benefit of fs laser processing is some unique surface morphology control. Dumitru et al. (2002) have shown that fs laser processing near the ablation threshold can produce surface ripples on ultrahard materials, including WC, which is of interest for tribological applications. Dumitru et al. also

* Corresponding authors.
E-mail addresses: smathaudhu@engr.ucr.edu (S. Mathaudhu), gaguilar@engr.ucr.edu (G. Aguilar).

measured for the first time the ablation threshold of bindered WC to be approximately 0.4 J/cm^2. After Dumitru et al.'s measurement, Byskov-Nielsen et al. (2010) also measured the single pulse ablation threshold for various materials and found tungsten (W) to have nearly the same threshold as Dumitru's bindered WC: 0.44 ± 0.02 J/cm^2. Developing effective techniques to machine binderless WC will broaden its use in many binder-caustic or extreme environment applications where bindered WC is currently used with limitations or unable to be used.

Femtosecond laser machining is a complex process that typically involves several mechanisms occurring across several timescales. The thermalization of absorbed fs laser energy and the mechanisms and timescales involved have been explained by von der Linde et al. (1997). A description of the mechanisms and corresponding two-temperature models were first reported in the literature by Anisimov et al. (1974) and then expanded upon by Nolte et al. (1997) as well as by Chen et al. (Chen et al., 2006), among others. However, several researchers have noticed a decrease in the ablation threshold, or an incubation effect, when studying multi-pulse fs ablation, for example of Mo thin films at 70 MHz (Cano-Lara et al., 2011) and stainless steel at 50–1000 kHz (Di Niso et al., 2014). Several reasons related to increased absorption due to structural defects (Neuenschwander et al., 2013) or surface roughness (Häfner et al., 2016) have been proposed, although few have studied incubation effects at MHz repetition rates. In addition to increased absorption, material thermal properties are known to vary with increasing temperature, although most models have assumed material properties to be constant. While it is difficult to probe *in-situ* temperature rise due to absorption of laser irradiation, irradiating well below the single pulse ablation threshold somewhat simplifies the processing mechanisms in play by removing variables of heat lost via ablated material, particle shielding, vaporization, plasma generation and the associated increase in absorption.

In many difficult-to-machine materials, such as WC, it is useful to know the minimum fluence at which ablation occurs so that non-ablative processes stay below that fluence threshold or so that texturing or machining-type processes stay above that threshold. Pfeiffer et al. (2011) measured the WC ablation threshold (0.38 J/cm^2) and determined the absorption coefficient to be 4.43·10^5 cm^{-1}. Surface roughness could be high enough to alter the reflectivity and absorption, however, to our knowledge none have reported ablation thresholds as a function of initial surface roughness. In addition, there have been reports that a WC binder phase may have a different ablation threshold than the WC phase. Pham et al. (2013) drilled holes in cemented (or bindered) tungsten carbide (cobalt carbide) with fs laser pulses and noted the formation of pores on the side walls of the holes suggesting the preferential removal of cobalt during fs laser drilling. Dumitru et al. also claimed cobalt binder was ablated before WC particles due to its lower melting temperature, however no other systematic studies on the effect of cobalt binders on ablation threshold have been reported.

Beyond the effects of surface roughness and the presence of metal binders in WC on the ablation threshold, the microstructure may influence laser ablation dynamics. For fluences well above the single pulse ablation threshold, phase boundaries and voids may influence the ablated particle size and morphology. However, for ablation well below the single pulse threshold, grain size may affect thermal diffusivity and conductivity, which significantly affects heat accumulation (HA) at high repetition rate irradiation. Perecherla and Williams (1988) reported that higher binder content, between 1.5 and 30 wt% Co, in bindered WC lowers thermal conductivity, from about 90 to about 45 W·m^{-1} K^{-1}, due to electron and phonon scattering by carbon (C) and W atoms presumably in solid solution in the binder phase. Upadhyaya (2001) and Wang et al. (2015) further confirmed this trend and Wang et al. found thermal conductivity in Co-bindered WC to increase with grain size from 1.5 to 9 μm range. Perecherla and Williams using different techniques showed thermal conductivity to increase with grain sizes in the 1.2 to 5.5 μm range at room temperature, which is due to fewer grain boundaries scattering phonons. While the

literature reports do not present a full perspective of the complex microstructural effects on ablations thresholds, it can be generally deduced that defects which affect thermal conductivity will thereby also affect heat accumulation in high repetition rate laser irradiation.

To explore the machinability of binderless WC via laser micromachining as compared to Co-bindered WC, we report on the ablation behavior of these materials under high repetition rate, ultra-low-fluence fs laser irradiation. HA-ablation spots developed after milliseconds (ms) of laser exposure on polished, fine-grained binderless and Co-binder WC materials. A better understanding of the ablation mechanisms and incubation effects at these irradiation conditions and sample microstructures will help forecast the feasibility of using ultrafast laser processing for relatively precise and fast machining of WC while avoiding shielding effects and multi-pulse heat accumulation. It will also help forecast the ability to replace bindered WC with binderless counterparts in more demanding environments.

2. Methods

2.1. Material preparation

Binderless WC samples were densified with Current Activated Pressure Assisted Densification (CAPAD), a process previously described extensively in (Garay, 2010). This technique allows the consolidation of near unity relative density bulk materials at low temperatures, enabling the production of fine grained binderless WC, which cannot be made with traditional free-sintering, or liquid-phase sintering approaches. For this study, commercially available binderless WC powder (TaeguTac, 99.95% purity, 500 nm grain size) samples were prepared. Each sample was heated at 300 °C/min until reaching hold temperature, and then held for 300 s at the maximum temperature. To vary relative density (void fraction), hold temperatures of 1400, 1500, 1600, 1700 and 1800 °C were used. Throughout the heating cycle, a maximum pressure of 60 MPa was uniaxially applied. After densification, the samples were mechanically polished using silicon carbide paper (600, 800, 1200 grit) and suspended alumina particles (9, 1, 0.05 μm). Commercially available (Ohio Carbon Blank, Columbus, OH) 800 nm grain size WC-10 wt% Co (hereafter "bindered" or WC-10Co) samples were also polished in the same steps. All samples were ~ 2 mm thick after polishing and 19 mm in diameter.

2.2. Irradiation conditions

The laser used for the experiments was an Amplitude Systems MIKAN Ytterbium doped Ti:Sapphire-based system delivering 230 fs pulses at a central wavelength of 1028 nm. The beam was focused perpendicular to the sample surface using an achromatic lens with a focal length of 18 mm. A Gaussian FWHM spot size diameter of 16 μm was used for all experiments. The repetition rate of the laser was 54.7 MHz, measured by photodiode DC-coupled to a 1 MΩ oscilloscope. An electro-mechanical shutter was applied to get the desired exposure times; 0.10, 0.20, 0.50, 1.00, 2.00 and 5.00 s for these experiments (Figs. 2 and 3). A half waveplate and polarizer were used to attenuate the average laser power, which was set to 200, 300, 400, 500, 600, 700, 800, 900 and 1000 mW with a calibrated power meter. The pulse energy is derived by dividing the average power by the laser repetition rate. The resulting applied pulse energies used were 3.66, 5.48, 7.31, 9.14, 11.0, 12.8, 14.6, 16.5 and 18.3 nJ. Fluences were calculated as pulse energy divided by spot area, and were 1.82, 2.73, 3.64, 4.55, 5.46, 6.37, 7.27, 8.18 and 9.09 mJ/cm^2, respectively.

In addition to generating HA-ablation in fixed locations, microchannel grooves were machined using fluences near HA-ablation thresholds to study the effect of scanning speed on heat accumulation and machining morphology. Microchannel grooves were machined on the sample surfaces by translating the samples perpendicular to the beam at speeds of 0.10, 0.25, 0.50, 0.75 and 1.00 mm/s. Light

microscopy images were taken of grooves irradiated over a length of 1000 μm (see Fig. 4) with 150 μm separation between the five parallel scanning speeds grooves.

Using a power meter to measure the reflected laser light after polishing, the binderless WC was measured to have approximately 36% reflectance and WC-10Co WC 35%. Reflectance measurements on samples polished with 600 and 800 grit silicon carbide paper enabled the verification of polishing to a sufficient and consistent level (1200 grit or 9 μm suspended alumina) to achieve mostly specular reflection. Diffuse reflection was obvious in samples that were polished with 600 grit silicon carbide paper, which was the coarsest polish used in our sample preparation. The HA-ablation and micromachining experiments were conducted on samples that had been polished with 1 μm alumina particles suspended in felt with water to minimize surface roughness effects.

Light microscopy helped to qualify the surface finish and initial laser ablations. Scanning electron microscopy (SEM) was performed on a FEI NNS450 and was used to determine the areas of the HA-ablation and heat affected zones (Fig. 2). The height and depth of the ablated surface structures (Fig. 3) are found using an AIST-NT atomic force microscope (AFM). The groove profiles (Fig. 4) were measured using a Dektak profilometer with a 200-nm diamond tip. Hardness and fracture toughness from Vickers indentation, following Anstis et al. (1981) were obtained from a Nanovea mechanical tester. Thermal diffusivity (α) was found using photothermal radiometry, after Martínez-Torres et al., (2009), specific heat capacity (C_p) was measured using a thermogravimetric analysis-differential scanning calorimeter (TGA-DSC), and density (ρ) was found using Archimedes method; the product of these three gives thermal conductivity (k).

3. Results

3.1. Thermal and mechanical properties

The increased densification temperature has multiple effects on sample properties through control of the void fraction, or density relative to full theoretical density of 15.66 g/cm³ (Page et al., 2008) (ICSD code 246149). As expected, increased density correlates with increased hardness, increased K_{IC} fracture toughness, and increased thermal diffusivity. Only WC densified at 1600, 1700, and 1800 °C (hereafter WC_{1600}, WC_{1700}, WC_{1800}) were judged to be of sufficient density to be used for laser irradiation testing. The thermal conductivity derived from the measurements in Fig. 1 are 52.9, 52.0 and 51.3 W·m⁻¹ K⁻¹ for WC_{1800}, WC_{1700} and WC_{1600}, respectively. Thermal conductivity of the commercial composite ceramic-metal WC-10Co follows a rule of mixtures between the binder and hard phase and although not measured, is expected to match typical commercial WC-Co

conductivity values between 80 and 100 W·m⁻¹ K⁻¹.

Kim et al. (2006) also used field-assisted sintering (a process analogous in all but name to the CAPAD process) to produce binderless WC and reported 27.99 GPa Vickers hardness (10 kg$_f$) and 7.1 MPa m$^{1/2}$ fracture toughness, after Anstis et al. (1981), for 0.38 μm grain size. Bľanda et al. (2015) have studied the indentation hardness of the cemented WC constituents showing a significant influence of the crystallographic orientation of WC crystals, which, along with possible local void concentration under the indentation tip, increases the standard deviation error bars of hardness measurements in Fig. 1.

3.2. Heat accumulation-ablation spot characterization

In opaque materials, the lateral spot size dimensions (tens of μm) are commonly much longer than the optical penetration depth, (a few nanometers), primarily resulting in lateral diffusion of heat and ultimately generating a heat affected zone (HAZ) outward radially, as seen in Fig. 2. The threshold to develop a HAZ is evidently lower than HA-ablation and gives some insight of temperature distribution. HAZ threshold is observed with only microscopy, while the ablation zones are observable by microscopy and surface profilometry. Both types of areas are measured using SEM images with a brightness gradient filter fit to an ellipse. The fluence was varied by adjusting the laser power rather than by changing the spot size. The exposure times (left to right in Fig. 2) correspond to roughly 5.47, 10.9, 27.4, 54.7, 109 and 274 million pulses, respectively.

In all four samples (WC-10Co, WC_{1800}, WC_{1700}, WC_{1600}), spots irradiated less than 2.00 s with 2.73 mJ/cm² fluence do not exhibit ablated area clearly via SEM, but still have a HAZ. As shown by the blue filled data in Fig. 2, the HA-ablation threshold is crossed somewhere between 1.00 and 2.00 s of exposure at 2.73 mJ/cm² fluence for WC_{1700}. With SEM, WC_{1600}, WC_{1800} and WC-10Co also appear to cross the ablation threshold between 1.00 and 2.00 s of exposure at 2.73 mJ/ cm², but other exposure time/threshold fluence combination thresholds are observed for the same samples and listed in Table 1. For example, from AFM the ablation threshold for WC_{1600} is between 0.10 and 0.50 s of exposure at 4.55 mJ/cm² fluence (Fig. 3) and for WC-10Co it is near 0.10 s of exposure at 3.64 mJ/cm² (not shown). Fig. 2 shows the areas of the ablated spots and their corresponding HAZ for WC_{1700} irradiated with fluences of 2.73, 4.55 and 9.09 mJ/cm² for exposure times between 0.10 and 5.00 s.

Similar HA-ablation area behavior is observed between the three binderless WC samples, but the corresponding heat affected areas are largest on WC_{1600} and smallest on WC_{1800}, which is inversely related to the ordering of their thermal conductivities. We hypothesize that larger thermal conductivity results in larger heat dissipation and therefore smaller observed surface HAZ. WC-10Co HA-ablation areas are larger
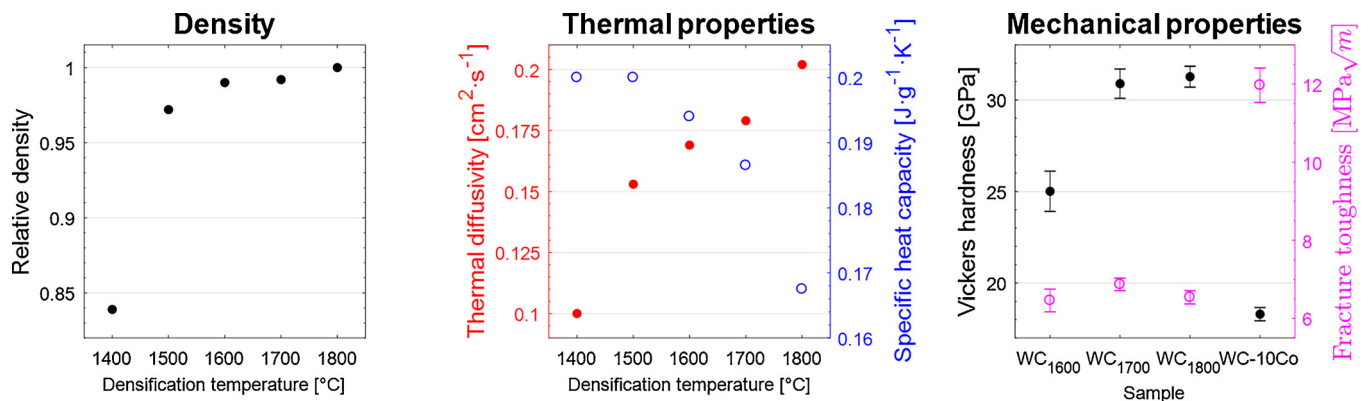

Fig. 1. Relative density (left), thermal diffusivity (center filled) and specific heat capacity (center open) of WC samples densified at 1400, 1500, 1600, 1700 and 1800 °C. Vickers hardness (right filled) and fracture toughness (right open) of WC samples densified at 1600, 1700 and 1800 °C compared to commercially available cemented WC-10Co. Error bars show standard deviation of twenty tests, otherwise data points represent a single measurement.
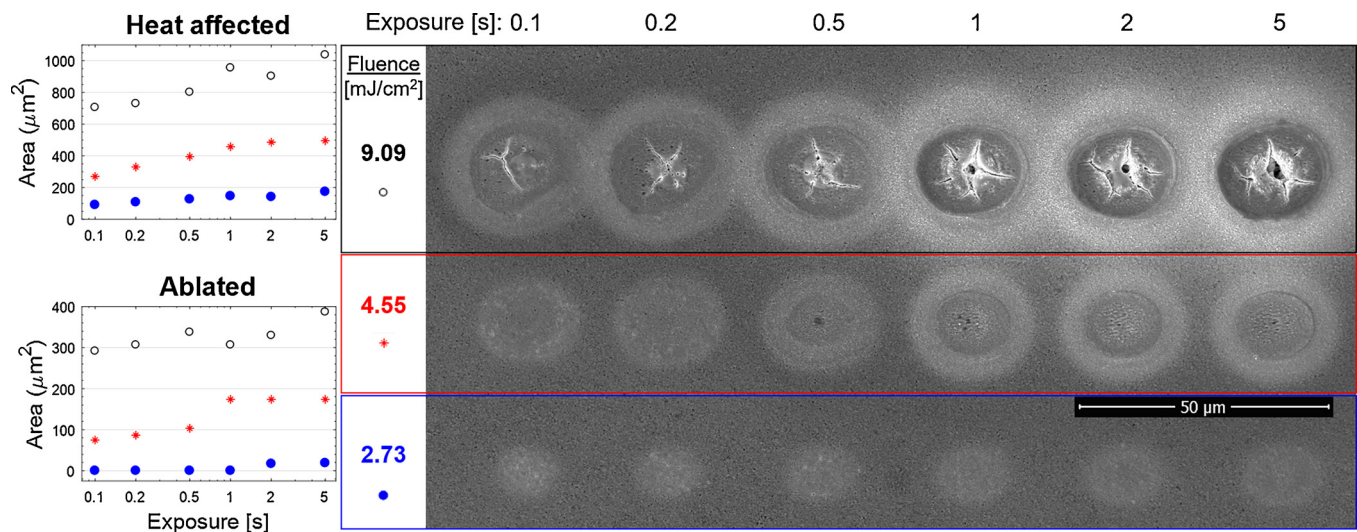
Fig. 2. WC_{1700} secondary electron SEM image and area measurements using a brightness gradient filter fit. Heat affected area (top left) includes any ablated area (bottom left) that developed inside the heat affected area. Fluences of 9.09 (black open), 4.55 (red asterisk) and 2.73 (blue filled) mJ/cm^2 are shown and measured for laser exposure times of 0.10, 0.20, 0.50, 1.00, 2.00 and 5.00 s. (For interpretation of the references to colour in this figure legend, the reader is referred to the web version of this article.)

than the corresponding binderless WC areas at $2.73 \, mJ/cm^2$ fluence, but generally smaller at 4.55 and $9.09 \, mJ/cm^2$ fluences, while the crown area is generally larger. This may be related with the melting of the Co binder phase at a lower temperature (1495 °C) than the WC phase (2720 °C). Because thermal energy is dissipated faster in our WC-10Co sample, the HAZ is comparatively smaller, but at the lower threshold fluence of $2.73 \, mJ/cm^2$ the melting area is greater due to the presence of a lower melting point phase (10 wt% Co). However, at the higher fluences of $4.55 \, mJ/cm^2$ a few non-mutually exclusive possibilities may help explain the smaller HA-ablation areas of bindered WC. One is that the WC phase melting begins to dominate, and another is that temperatures high enough to evaporate Co are reached (2925 °C), still another is that the binder phase, once melted, spreads to cover a larger fraction of the surface at the irradiation spot and reduces the absorption. Further studies that include chemical analysis should help clarify these possibilities. The WC-10Co sample did not crack at $9.09 \, mJ/cm^2$ fluence for any exposure time up to 5 s. However, due to

their lack of binder, lower toughness and higher hardness, all three binderless samples locally fracture at 0.50 s and longer exposures at $9.09 \, mJ/cm^2$, as seen in the top row of Fig. 2.

Fig. 3 shows the AFM height scans of the tungsten carbide surface after controlled exposure times. These spots correspond to experiments performed on the same sample surface as the experiments shown in Fig. 2. Note that the height is exaggerated to better show surface height variations in conjunction with a height color scale showing darker shades as lower and lighter shades as higher. The raised crown exhibited around all the spots irradiated above HA-ablation threshold is commonly seen in surfaces that have melted, typically from longer pulse length (ns) lasers. This raised ring suggests melting is occurring due to heat accumulation in our samples.

Among binderless WC, WC_{1800} with the highest thermal conductivity, has the most sensitivity to the exposure times required for HA-ablation: between 1.00 and 2.00 s at a fluence of $2.73 \, mJ/cm^2$, 0.10 and 0.50 s at $3.64 \, mJ/cm^2$ and less than 0.10 s at $4.55 \, mJ/cm^2$. The

Table 1
Laser parameters of ultrafast ablation threshold in tungsten carbide materials.

Material	Grain size	Irradiance parameters			Pulse parameters		
		Fluence	Exposure time	Rep rate	Energy	Length	Ablation type
Binderless WC_{1600}[a]	0.5 μm	$2.73 \, mJ/cm^2$	~500 ms	54.7 MHz	5.48 nJ	230 fs	Heat accumulation
		$3.64 \, mJ/cm^2$	~500 ms	54.7 MHz	7.31 nJ	230 fs	Heat accumulation
		$4.55 \, mJ/cm^2$	100-500 ms	54.7 MHz	9.14 nJ	230 fs	Heat accumulation
		$5.46 \, mJ/cm^2$	< 100 ms	54.7 MHz	11.0 nJ	230 fs	Heat accumulation
Binderless WC_{1700}[a]	0.5 μm	$2.73 \, mJ/cm^2$	1.00-2.00 s	54.7 MHz	5.48 nJ	230 fs	Heat accumulation
		$3.64 \, mJ/cm^2$	~500 ms	54.7 MHz	7.31 nJ	230 fs	Heat accumulation
		$4.55 \, mJ/cm^2$	100-500 ms	54.7 MHz	9.14 nJ	230 fs	Heat accumulation
		$5.46 \, mJ/cm^2$	< 100 ms	54.7 MHz	11.0 nJ	230 fs	Heat accumulation
Binderless WC_{1800}[a]	0.5 μm	$2.73 \, mJ/cm^2$	1.00-2.00 s	54.7 MHz	5.48 nJ	230 fs	Heat accumulation
		$3.64 \, mJ/cm^2$	100-500 ms	54.7 MHz	7.31 nJ	230 fs	Heat accumulation
		$4.55 \, mJ/cm^2$	< 100 ms	54.7 MHz	9.14 nJ	230 fs	Heat accumulation
WC-10Co[a]	0.8 μm	$2.73 \, mJ/cm^2$	100-500 ms	54.7 MHz	5.48 nJ	230 fs	Heat accumulation
		$3.64 \, mJ/cm^2$	~100 ms	54.7 MHz	7.31 nJ	230 fs	Heat accumulation
		$4.55 \, mJ/cm^2$	< 100 ms	54.7 MHz	9.14 nJ	230 fs	Heat accumulation
WC-10Co[b]	0.5 μm	$0.4 \, J/cm^2$	150 fs	1 kHz	2.8–54 μJ	150 fs	Single pulse
WC-6Co[b]	1.5 μm	$0.3 \, J/cm^2$	150 fs	1 kHz	2.8–54 μJ	150 fs	Single pulse
WC (unspecified)[c]	–	$0.38 \, J/cm^2$	150 fs	1 kHz	8.8 μJ	150 fs	Single pulse

[a] This work.
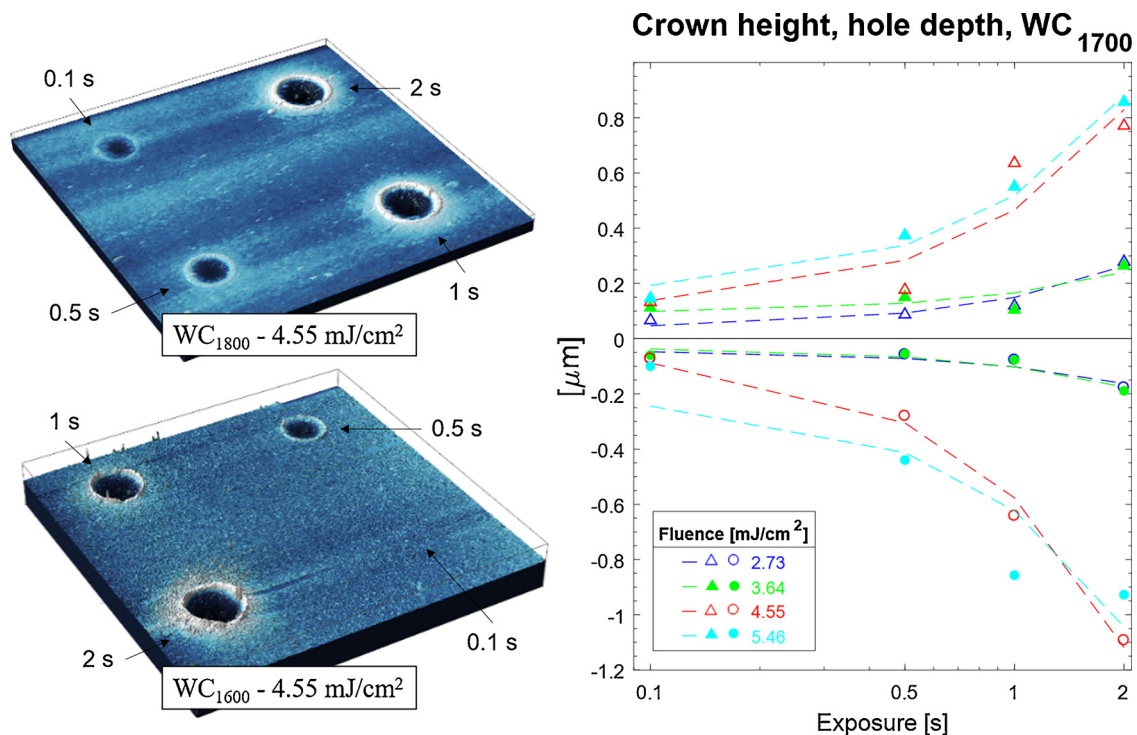[b] (Dumitru et al., 2002) and.
[c] (Pfeiffer et al., 2011).

Fig. 3. AFM 3D representation of HA-ablation spots on binderless WC_{1800} (top left) and WC_{1600} (bottom left) with 4.55 mJ/cm^2 for 0.10, 0.50, 1.00 and 2.00 s exposure (height exaggerated). There is no crown or ablation evident in WC_{1600} or WC_{1700} after only 0.10 s of exposure at 4.55 mJ/cm^2 fluence. The height trends of WC_{1700} spots exhibiting crowns surrounding ablated volumes is plotted (right). Triangles show the highest points in each crown and circles show the lowest points in each hole for fluences of 2.73 (blue), 3.64 (green), 4.55 (red), and 5.46 (cyan) mJ/cm^2. Dashed trendlines are shown to help distinguish between overlapping data markers. (For interpretation of the references to colour in this figure legend, the reader is referred to the web version of this article.)

WC_{1700} sample ablates between 1.00 and 2.00 s with a fluence of 2.73 mJ/cm^2. The WC_{1600} sample, with the lowest thermal conductivity of the binderless samples, ablates near 0.50 s at 2.73 and 3.64 mJ/cm^2 fluences, and between 0.10 and 0.50 s at 4.55 mJ/cm^2. This behavior perhaps expected in terms of thermal conductivity, but experiments with higher exposure time resolution would better elucidate the exposure time sensitivity behavior. Relative to the average height of the area immediately around the irradiation spot, we summarize the lowest point and highest point, wherever they may be, in each irradiated spot and crown area in the plot of Fig. 3. The AFM surface roughness on our polished samples hovers around 100 nm, which explains why even though there was no ablation observed on WC_{1700} after 0.10 s of exposure for fluences below 5.46 mJ/cm^2, there is still around 100 nm of crown height and hole depth plotted in Fig. 3. The WC-10Co sample crowns did not rise beyond 500 nm above the surrounding surface, which can be explained by the presence of Co evaporating away and/or helping to flow and flatten the semi-melted WC particles while molten. The hole depths of the WC-10Co matched the binderless WC samples in reaching around 1 µm depth at 2 s exposure but required 6.37 mJ/cm^2 fluence compared to 4.55 mJ/cm^2 for the three binderless samples.

3.3. Irradiated grooves characterization

The light microscopy surface morphology images, as seen in Fig. 4, show the difference between HA-ablation with (i.e. WC_{1700} with 8.64 mJ/cm^2 fluence at 0.10 mm/s scan speed) and without accompanied ejected debris along the groove edges. The cross-sectional width and shape of the laser-cut grooves is inconsistent between profilometry scans, likely due to a somewhat stuttered scanning velocity over time as the stepper motors jog from step to step during laser processing. Translation stages with more smooth velocity are expected to improve the groove profile consistency. Although various profiles along the same sample at the same speed and fluence are not shown, their

statistically varying widths, depths and roughness's are supported by what appears as overlapping spots in the binderless WC surface groove images shown in Fig. 4. The groove profiles shown in Fig. 4 were selected from at least five profiles of each sample to highlight a relatively ideal cutting cross section profile: high ablation to recast ratio, clean material removal in the groove, and high aspect ratio groove. In Fig. 4, the profile shown at 0.25 mm/s (red) is much wider than the other profiles shown due to the relatively large fluence (9.09 mJ/cm^2) and slow scan speed.

The cross-sectional area of the laser machined grooves (darker shade) and the melted recast peaks (lighter shade) was measured for the profiles in Fig. 4 and is reported to the right of each profile, highlighted for recast and boxed for ablated. Slower scan speeds and higher fluences yield larger HA-ablation to recast volume ratios.

For the same scanning speeds, bindered WC exhibit about half the continuous groove HA-ablation threshold fluence (4.55 mJ/cm^2) of the binderless counterparts (9.09 mJ/cm^2). This is perhaps not expected when compared with the fixed-location HA-ablation thresholds, but again explained by the presence and preferential melting ablation of the lower melting point binder phase. This hypothesis can be supported by our observation of the larger recast kerf cross section area of the WC-10Co sample when compared to the binderless WC samples at the same translation and fluence conditions. The higher CAPAD processing temperature of the binderless WC corresponds with slightly more ablated cross-sectional area at the same fluence and scanning speed. These results agree with the general observation that higher thermal conductivity samples exhibit HA-ablation at lower fluences when translating the samples. All the groove profiles ablation widths were less than or equal to the laser spot size while the recast widths could extend beyond the laser spot size up to about 10 µm radially.
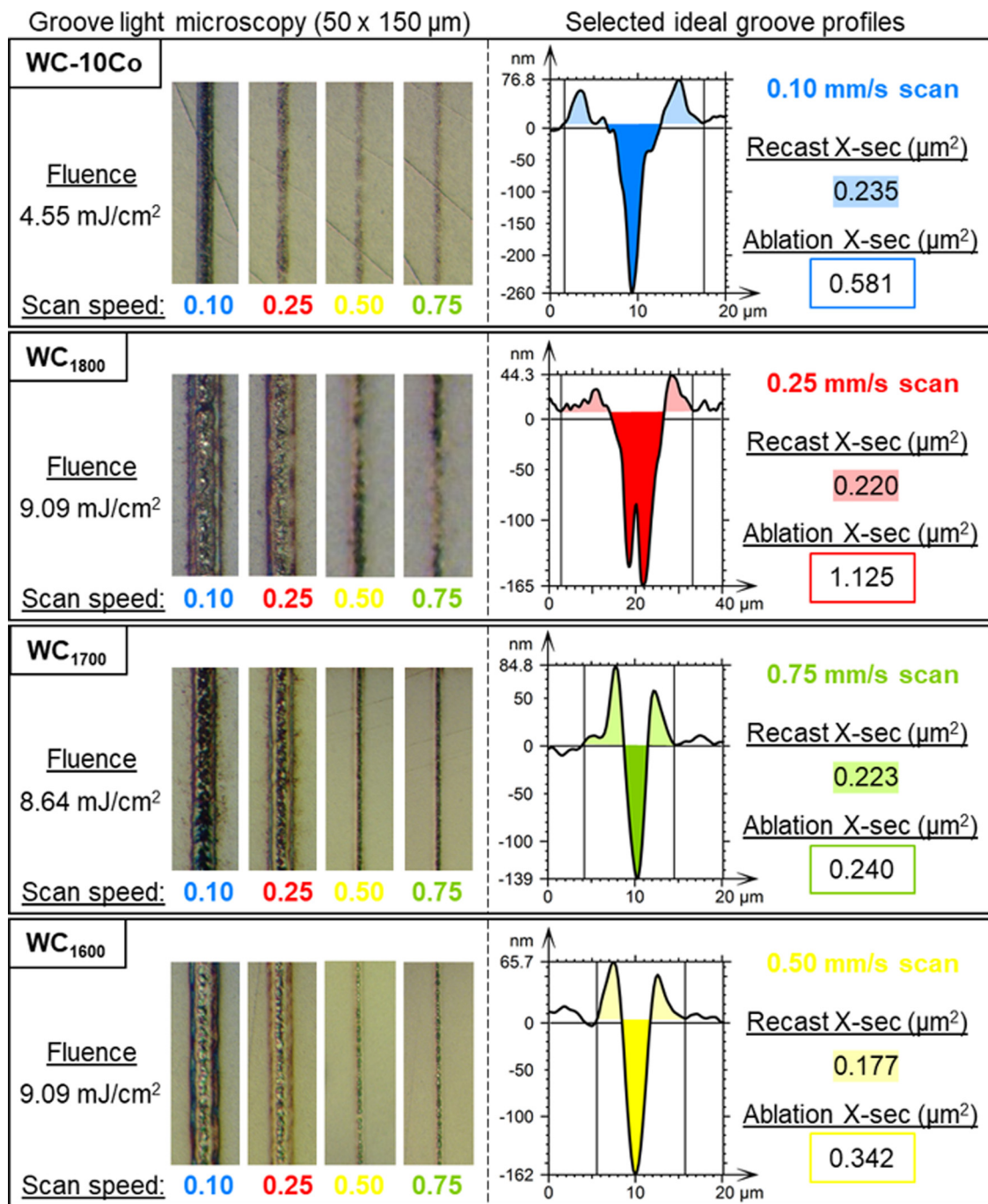
Fig. 4. Light microscopy images of the WC-10Co, WC_{1800}, WC_{1700} and WC_{1600} sample surfaces irradiated with the fluences labeled (left). Each sample has a selected groove profile shown (right), selected for high ablation volume and aspect ratio, at one of four color-coded scan speeds: 0.10 mm/s (blue), 0.25 mm/s (red), 0.50 mm/s (yellow), 0.75 mm/s (green). The profiles exhibit recast regions (lighter shade) on either side of the ablated groove (darker shade), which have cross sectional area reported to the right of the corresponding profile for both recast (highlighted) and ablated (boxed) areas. Note the z scale is in nm to show detail. (For interpretation of the references to colour in this figure legend, the reader is referred to the web version of this article.)

4. Discussion

4.1. Context of multi-pulse laser ablation

Laser ablation can be categorized into thermal and nonthermal. Pulses longer than a ns typically cause absorbing samples to increase in thermal energy to melting temperature before significant ablation occurs through other mechanisms. With the development of ultrafast pulse systems, Liu et al (1997) and others found the HAZ could be reduced or even eliminated. Fujimoto et al. (1984) were early to report

that electrons excited by pulses shorter than or equal to electron-phonon energy relaxation time are temporarily not in thermal equilibrium with the lattice. With sufficient energy, as in ultrafast single pulse ablation measurements, these nonequilibrium electrons lead to so-called nonthermal ablation mechanisms, which incidentally, is not observed in this study.

If fluence is above the single pulse ablation threshold, material ablated from the previous pulse will remove thermal energy along with the ablated particles, which complicates models trying to account for thermal effects. When fluence is below the single pulse ablation

threshold, then there is a possibility for heat to accumulate from pulse-to-pulse in the material without removal via ablation. The condition for heat to accumulate is that the time for thermalized laser irradiation to diffuse out of the focal volume must be shorter than the pulse cycle time. With an ultrashort and MHz repetition rate laser pulse train below the nonthermal single pulse ablation threshold, we may often find that the time between pulses is shorter than the time to diffuse heat out of the focal volume and therefore that heat is accumulating in the lattice. If we use experimental values to help us estimate this thermal relaxation time, after Bejan (1993) (18.43)

$$\tau_{thermal} \approx L_p^2 \big/ 2\alpha \qquad (1)$$

where L_p is the thermal penetration length and α is the thermal diffusivity, we can estimate if we are accumulating heat. Using 10 μm for the penetration length, conservatively based on the maximum range of visible HAZ (heat is diffused much further than what is visible on SEM of surface) of Fig. 2 for WC_{1700}, and 0.18 cm^2/s diffusivity for WC densified at 1700 °C from Fig. 1, we get a relaxation time of 2.8 μs (μs). This relaxation time is much longer than the time between pulses of our laser system (1/54.7 MHz) of 18.3 ns, thereby supporting a heat accumulation effect between successive pulses. Furthermore, if τ was 2.8 μs for a given material, the transition from thermal diffusion to heat accumulation would occur near 360 kHz (1/2.8 μs).

Literature reports a few examples of ultrafast ablation thresholds below the single pulse ablation threshold with high repetition rates. It has been reported previously by Eaton et al. (2008) that there is a transition from thermal diffusion to heat accumulation with 300–700 fs pulses at about 500 kHz in borosilicate glass, which has a softening temperature of 985 °C. While a 54.7 MHz repetition rate, more than 10 times higher than the highest repetition rate examined by Eaton (5 MHz) may seem to be too high to measure HA over a few seconds of irradiation, WC materials have about 50 times the thermal conductivity of borosilicate glass, so heat is dissipated much faster. Eaton et al. demonstrated that HA in borosilicate glass, albeit in the context of waveguide writing, is influenced by repetition rate, pulse energy, changes in absorption and state, and scanning speed. Along with heat accumulation, significantly lower ablation thresholds, on the order of mJ/cm^2, have been reported recently with ultrafast multi-pulse irradiation. In a report where heat accumulation conditions are likely met, Cano-Lara et al. (2011) observed high repetition rate (70 MHz) laser ablation of 500 nm thin film molybdenum on a fused silica substrate to be about one-fourth the previously reported laser ablation threshold fluence. This was attributed to thermal incubation effects. Cano-Lara measured a ~ 30 mJ/cm^2 threshold on a thin film (800 nm, 60 fs, ~ 2.4 nJ pulses), which is one order of magnitude higher than reported in this work. It is evident that repetition rate, material thermal properties, and nonlinear effects may all play a role in the incubation effects reported. A list of WC materials in Table 1 shows the variance of irradiation conditions that have been reported to achieve some type of ultrafast laser ablation, though thermal and optical properties of each material would aid completeness.

4.2. Summary of ultra-low fluence, ultrafast, multi-pulse laser heat accumulation and ablation

In the current study, non-thermal melting is not likely as it requires peak pulse intensities near 10^{12} W/cm^2, as discussed by (Rethfeld et al., 2004), while our experiments were conducted at 10^{10} W/cm^2. Instead, incident photons excite focal volume electrons on the timescale of the laser pulse (a few hundred fs) through absorption. On the next larger timescale, energy from recently excited electrons is transferred to the lattice (heating) a few ps after the pulse. The timescale of lattice heating due to electron-phonon collisions, as discussed by Rethfeld and others, is a few to tens of ps, and well within the temporal pulse spacing (10 ns to 1 μs for MHz laser systems). Keeping in mind the temporal pulse

spacing of our system is 18.3 ns, the time for complete thermal relaxation of the lattice must be greater than 18.3 ns for heat to accumulate, which our experimentally estimated thermal relaxation time of 2.8 μs is. Next, upon reaching melt temperature after sufficient laser exposure time, rapid material expansion and electrons excited beyond the Fermi level by multiphoton absorption cause particles to vacate the surface in all directions, typically leaving ejected particle debris and recently solidified particles nearby as seen in Fig. 4. The relatively slow melting ablation process of ions and particles in various degrees of melt moving away from the center of expansion occurs on the timescale of a few hundred ms, but this last step occurs only once the lowest melting point material phase is near the melting temperature from multi-pulse heat accumulation. The time required for the lattice temperature to reach melting temperature significantly depends on the absorption, fluence and material thermal conductivity. For the irradiation conditions of Figs. 2 and 3, the time before HA-melting is observed is on the order of hundreds of ms.

4.3. Heat accumulation modeling

If the material thermal and optical properties, as well as the laser parameters are known, temperature profiles in space and time can be calculated from various models. So far there is not a suitable model to fully represent the experimental conditions of this study. Nonetheless, as approximations to provide insight, several models were explored. The two-temperature model is a widely used approach for fs laser absorption and it uses separate electron and lattice heat conduction equations, which are coupled by the electron-phonon coupling constant. For example, Breitling et al. (2004) demonstrate that the two-temperature model gives good insight of the electron and lattice temperature rise at the ps and ns scales, estimating electron temperature rises on the order of thousands of K for typical single laser pulses of 1 ps or less. Although this model is useful for single pulse phenomena and promising for exploring incubation effects, to the best of our knowledge it has not yet been used in providing information about the laser-induced heating due to many successive ultrashort pulses.

A single temperature HA model proposed by Weber et al. (2014) estimates, with good experimental consistency in the case of drilling holes in CrNi-steel, the temperature HA due to multiple ultrashort pulses. Furthermore, in the case of 3D isotropic semi-infinite absorbing material, the HA is predicted to lead to a finite temperature with infinite number of pulses. Using material and laser values from this work (density = 15.66 × 10^3 kg/m^3, specific heat capacity = 167 J·kg^{-1} K^{-1}, thermal diffusivity = 2.00 × 10^{-5} m^2/s, reflectivity = 36%, repetition rate = 54.7 MHz) in the Weber model resulted in HA temperature increase convergence to 710 and 2362 °C for fluences of 2.73 and 9.09 mJ/cm^2, respectively. High repetition rate lasers are also referred to as quasi-continuous wave. As a contrast, a continuous wave laser-induced temperature model with the same average powers (300 and 1000 mW) used in the Weber model, irradiating on an isotropic semi-infinite absorbing material (Ready, 1971, eqn 3.17) results in steady state temperatures of 82 and 276 °C for fluences of 2.73 and 9.09 mJ/cm^2, respectively. The temperatures calculated by means of these two models seem low compared to our experimental melting results, considering the 2720 °C melting point of tungsten carbide reported by Dumitru et al. (2002). A model that adequately describes HA temperature induced by high repetition rate, ultrafast, multi-pulse laser pulse trains below ablation and melting thresholds is imminent, and this model should give insight into the mechanisms that govern these unique laser processing conditions.

4.4. Outlook and future work

In addition to the parameters explored in this study (thermal conductivity, machining speeds and exposure time), other parameters can be altered, as experimental equipment allow, to understand their

influence on ablation threshold and heat accumulation more fully in the ultra-low fluence, high repetition rate ablation regime. These include a broader range of material thermal conductivity, reflectivity/absorptivity, grain size, laser pulse length, wavelength and repetition rate. It is expected that further studies will help elucidate the fundamental mechanisms of incubation effects. Furthermore, quantification of laser micro-processing effects on materials such as WC is expected to lead to advances in tribological properties, surface appearance, wettability, or surface repair in a broad range of materials classes. To the best of our knowledge, the difference in heat accumulation due to multiphoton absorption versus single photon absorption has not been studied and may have unique applications in non-linear optics.

5. Conclusion

Through the application of MHz repetition rate, ultra-low fluence laser irradiation, we propose that laser ablation is achieved via melting from heat accumulation processes. This type of ultrafast ablation is different from non-thermal ultrafast single and multi-pulse ablation and different from thermal "slow" (non-ultrafast) single and multi-pulse melting-ablations. HA-ablation and micromachining at very low fluences and very low energies per pulse, yet at comparatively high repetition rates is demonstrated to be two orders of magnitude below non-thermal ultrafast single pulse ablation threshold fluence for similar materials. The crown and ridge structures formed around the irradiation spots and grooves, respectively, are likely due to recast melt expansion from heat accumulation during exposure to the high repetition rate pulse trains. With similar surface roughness, reflectance and grain size (800 nm with Co binder and 500 nm without binder), the Co bindered WC exhibited half the HA-ablation threshold fluence (4.55 mJ/cm^2) of its binderless counterparts (9.09 mJ/cm^2) while the samples were scanned at speeds between 0.10 and 1.00 mm/s. However, at lower fluence of 3.64 mJ/cm^2, if the samples and laser were not moving during exposure, they exhibited similar HA-ablation threshold between 100 and 500 ms of exposure. As expected, increased scanning speed reduced heat accumulation and resulted in less HA-ablation cross sectional area. Increased scanning speed also decreased ablation to recast cross sectional area ratio. Our results show preliminary evidence that small decreases in HA-ablation threshold correspond with increasing thermal conductivity (and the related density, hardness, and thermal diffusivity) for binderless WC. We hypothesize grain size affects HA-ablation only insomuch as it affects thermal conductivity. For the binderless samples, the heat affected areas are largest on WC_{1600} and smallest on WC_{1800}, which is inversely related to the ordering of their thermal conductivities. A few non-mutually exclusive possibilities may help explain the difference in HA-ablation areas between bindered and binderless WC. One is that there is a transition between which phase dominates ablation morphology: Co binder (1495 °C) to WC (2720 °C), another is that temperatures high enough to evaporate Co are reached (2925 °C), still another is that the binder phase, once melted, spreads to cover a larger fraction of the surface at the irradiation spot and reduces the absorption. Further studies that include chemical analysis and higher resolution exposure times should help clarify these possibilities. We hypothesize the lower melting point binder, Co, melts at lower fluence and is still well-adhered to nearby WC as it ablates, and results in lower recast crown heights. The presence and preferential removal of Co, also noticed by Pham et al. (2013) near the single pulse ablation threshold, is responsible for HA-ablation morphology differences with the binderless WC counterpart. In general, this ultralow fluence, MHz repetition rate laser ablation is not ideal for precise machining of ultrahard materials due to the heat affected zones and relatively slow removal rates, however, it forecasts promising ultrafast laser micromachinability of binderless WC for extreme environment applications at repetition rates below heat accumulation, which depend on the thermal relaxation time. The advantages of the micromachining approach used in this work would be for niche applications that desire

localized surface recrystallization or surface plasmonic effects, or for bandgap materials that desire nonlinear interaction simultaneous to localized annealing or melting, and finally for semiconductor materials surface geometry or defect concentration "fine-tuning".

References

Anisimov, S.I., Kapeliovich, B.L., Perel-man, T.L., 1974. Electron emission from metal surfaces exposed to ultrashort laser pulses. J. Exp. Theor. Phys + . 66, 375–377.

Anstis, G.R., Chantikul, P., Lawn, B.R., Marshall, D.B., 1981. A critical evaluation of indentation techniques for measuring fracture toughness: I, direct crack measurements. J. Am. Ceram. Soc. 64, 533–538. https://doi.org/10.1111/j.1151-2916.1981.tb10320.x.

Bejan, A., 1993. Heat Transfer. John Wiley & Sons, New York.

Bľanda, M., Duszová, A., Csanádi, T., Hvizdoš, P., Lofaj, F., Dusza, J., 2015. Indentation hardness and fatigue of WC – Co composites. Int. J. Refract. Met. Hard 49, 178–183. https://doi.org/10.1016/j.ijrmhm.2013.04.006.

Breitling, D., Ruf, A., Dausinger, F., 2004. Fundamental aspects in machining of metals with short and ultrashort laser pulses. Herman, P.R., Fieret, J., Piqué, A., Okada, T., Bachmann, F.G., Hoving, W., Washio, K., Xu, X., Dubowski, J.J., Geohegan, D.B., Träger, F. (Eds.), Photon Processing in Microelectronics and Photonics III, Proc. of SPIE 5339, 49–63. https://doi.org/10.1117/12.541434.

Byskov-Nielsen, J., Savolainen, J.M., Christensen, M.S., Balling, P., 2010. Ultra-short pulse laser ablation of metals: threshold fluence, incubation coefficient and ablation rates. Appl. Phys. A Mater. 101, 97–101. https://doi.org/10.1007/s00339-010-5766-1.

Cano-Lara, M., Camacho-López, S., Esparza-García, a., Camacho-López, Ma., 2011. Laser-induced molybdenum oxide formation by low energy (nJ)–high repetition rate (MHz) femtosecond pulses. Opt. Mater. 33, 1648–1653. https://doi.org/10.1016/j.optmat.2011.04.029.

Chen, J.K., Tzou, D.Y., Beraun, J.E., 2006. A semiclassical two-temperature model for ultrafast laser heating. Int. J. Heat Mass Transf. 49, 307–316. https://doi.org/10.1016/j.ijheatmasstransfer.2005.06.022.

Di Niso, F., Gaudiuso, C., Sibillano, T., Paolo, F., Ancona, A., Lugarà, P.M., 2014. Role of heat accumulation on the incubation effect in multi-shot laser ablation of stainless steel at high repetition rates. Opt. Express 22, 12200–12210. https://doi.org/10.1364/OE.22.012200.

Dumitru, G., Romano, V., Weber, H.P., Sentis, M., Marine, W., 2002. Femtosecond ablation of ultrahard materials. Appl. Phys. A Mater. 74, 729–739. https://doi.org/10.1007/s003390101183.

Eaton, S.M., Zhang, H., Ng, M.L., Li, J., Chen, W.-J., Ho, S., Herman, P.R., 2008. Transition from thermal diffusion to heat accumulation in high repetition rate femtosecond laser writing of buried optical waveguides. Opt. Express 16, 9443–9458. https://doi.org/10.1364/OE.16.009443.

Eberle, G., Wegener, K., 2014. Ablation study of WC and PCD composites using 10 picosecond and 1 nanosecond pulse durations at green and infrared wavelengths. Phys. Proc. 56, 951–962. https://doi.org/10.1016/j.phpro.2014.08.115.

Echlin, M.P., Straw, M., Randolph, S., Filevich, J., Pollock, T.M., 2015. The TriBeam system: femtosecond laser ablation in situ SEM. Mater. Charact. 100, 1–12. https://doi.org/10.1016/j.matchar.2014.10.023.

Farsari, M., Filippidis, G., Zoppel, S., Reider, G.A., Fotakis, C., 2007. Micromachining of silicon carbide using femtosecond lasers. J. Phys. Conf. Ser. 59, 84–87. https://doi.org/10.1088/1742-6596/59/1/018.

Fujimoto, J.G., Liu, J.M., Ippen, E.P., Bloembergen, N., 1984. Femtosecond laser inter-action with metallic tungsten and nonequilibirium electron and lattice temperatures. Phys. Rev. Lett. 53, 1837–1840.

Garay, J.E., 2010. Current-activated, pressure-assisted densification of materials. Annu. Rev. Mater. Res. 40, 445–468. https://doi.org/10.1146/annurev-matsci-070909-104433.

Häfner, T., Heberle, J., Dobler, M., Schmidt, M., 2016. Influences on incubation in ps laser micromachining of steel alloys. J. Laser Appl. 28, 022605. https://doi.org/10.2351/1.4944445.

Jahan, M.P., Rahman, M., Wong, Y.S., 2011. A review on the conventional and micro-electrodischarge machining of tungsten carbide. Int. J. Mach. Tool. Manuf. 51, 837–858. https://doi.org/10.1016/j.ijmachtools.2011.08.016.

Kim, H.C., Yoon, J.K., Doh, J.M., Ko, I.Y., Shon, I.J., 2006. Rapid sintering process and mechanical properties of binderless ultra fine tungsten carbide. Mater. Sci. Eng. A Struct. 435–436, 717–724. https://doi.org/10.1016/j.msea.2006.07.127.

Liu, X., Du, D., Mourou, G., 1997. Laser ablation and micromachining with ultrashort laser pulses. IEEE J. Quantum Electron. 33, 1706–1716. https://doi.org/10.1109/3.631270.

Martínez-Torres, P., Mandelis, A., Alvarado-Gil, J.J., 2009. Photothermal determination of thermal diffusivity and polymerization depth profiles of polymerized dental resins. J. Appl. Phys. 106, 114906. https://doi.org/10.1063/1.3266007.

Neuenschwander, B., Jaeggi, B., Schmid, M., Dommann, A., Neels, A., Bandi, T., Hennig, G., 2013. Factors controlling the incubation in the application of ps laser pulses on copper and iron surfaces. Xu, X., Hennig, G., Nakata, Y., Roth, S.W. (Eds.), Laser Applications in Microelectronic and Optoelectronic Manufacturing XVIII, Proc. of SPIE 8607, 1–10. https://doi.org/10.1117/12.2004136.

Nolte, S., Momma, C., Jacobs, H., Tünnermann, A., Chichkov, B.N., Wellegehausen, B., Welling, H., 1997. Ablation of metals by ultrashort laser pulses. J. Opt. Soc. Am. B 14, 2716–2722.

Page, K., Li, J., Savinelli, R., Szumila, H.N., Zhang, J., Stalick, J.K., Proffen, T., Scott, S.L., Seshadri, R., 2008. Reciprocal-space and real-space neutron investigation of nanos-tructured Mo2C and WC. Solid State Sci. 10, 1499–1510. https://doi.org/10.1016/j.solidstatesciences.2008.03.018.

Perecherla, A., Williams, W.S., 1988. Room-temperature thermal conductivity of ce-mented transition-metal carbides. J. Am. Ceram. Soc. 71, 1130–1133.

Pfeiffer, M., Engel, A., Weißmantel, S., Scholze, S., Reisse, G., 2011. Microstructuring of steel and hard metal using femtosecond laser pulses. Phys. Proc. 60–66. https://doi.org/10.1016/j.phpro.2011.03.106.

Pham, K.X., Tanabe, R., Ito, Y., 2013. Laser-induced periodic surface structures formed on the sidewalls of microholes trepanned by a femtosecond laser. Appl. Phys. A Mater. 112, 485–493. https://doi.org/10.1007/s00339-012-7437-x.

Ready, J.F., 1971. Effects of High-Power Laser Radiation. Academic Press, Inc., New York.

Rethfeld, B., Sokolowski-Tinten, K., von der Linde, D., Anisimov, S.I., 2004. Timescales in the response of materials to femtosecond laser excitation. Appl. Phys. A Mater. 79, 767–769. https://doi.org/10.1007/s00339-004-2805-9.

Sugioka, K., Cheng, Y., 2014. Femtosecond laser three-dimensional micro- and nano-fabrication. Appl. Phys. Rev. 1, 041303. https://doi.org/10.1063/1.4904320.

Upadhyaya, G.S., 2001. Materials science of cemented carbides—an overview. Mater. Des. 22, 483–489.

von der Linde, D., Sokolowski-Tinten, K., Bialkowski, J., 1997. Laser–solid interaction in the femtosecond time regime. Appl. Surf. Sci. 109–110, 1–10. https://doi.org/10.1016/S0169-4332(96)00611-3.

Wang, H., Webb, T., Bitler, J.W., 2015. Study of thermal expansion and thermal con-ductivity of cemented WC-Co composite. Int. J. Refract. Met. Hard 49, 170–177. https://doi.org/10.1016/j.ijrmhm.2014.06.009.

Weber, R., Graf, T., Berger, P., Onuseit, V., Wiedenmann, M., Freitag, C., Feuer, A., 2014. Heat accumulation during pulsed laser materials processing. Opt. Express 22, 11312–11324. https://doi.org/10.1364/OE.22.011312.